Journal of Power Sources 216 (2012) 249–255

Contents lists available at SciVerse ScienceDirect

Journal of Power Sources

journal homepage: www.elsevier.com/locate/jpowsour

Direct synthesis of oxygen-deficient Li_2MnO_{3-x} for high capacity lithium battery electrodes

Kei Kubota [a], Takayuki Kaneko [a], Masaaki Hirayama [a], Masao Yonemura [b], Yuichiro Imanari [c], Kenji Nakane [c], Ryoji Kanno [a,*]

[a] Department of Electronic Chemistry, Interdisciplinary Graduate School of Science and Engineering, Tokyo Institute of Technology, 4259 Nagatsuta-cho, Midori-ku, Yokohama 226-8502, Japan
[b] Neutron Science Laboratory, Institute of Materials Structure Science, High Energy Accelerator Research Organization, 1-1 Oho, Tsukuba, Ibaraki 305-0801, Japan
[c] Tsukuba Material Development Laboratory, Sumitomo Chemical Co., Ltd., 6 Kitahara, Tsukuba 300-3294, Japan

HIGHLIGHTS

- The new oxygen deficient phase was directly synthesized by reduction treatment.
- The phase showed reversible oxygen insertion and extraction.
- A 1st discharge capacity of 305 mAh g^{-1} without a 1st charge plateau above 4.4 V.

ARTICLE INFO

Article history:
Received 10 May 2012
Accepted 22 May 2012
Available online 30 May 2012

Keywords:
Lithium batteries
Layered cathode material
Lithium manganese oxide
Metal hydride
Anomalous capacity
Li_2MnO_3

ABSTRACT

Oxygen-deficient Li_2MnO_{3-x} ($0 < x < 0.19$) have been directly synthesized from lithium-rich manganese oxide, Li_2MnO_3, using metal hydrides (CaH_2 and LiH) as reducing agents at reaction temperatures of 255–265 °C. The structure of the reduced phase determined by X-ray diffraction experiments has oxygen vacancies in the layered structure, causing slightly larger lattice parameters than the stoichiometric Li_2MnO_3. Reversible oxygen insertion and extraction from the deficient structure observed by the TG measurements suggests fast oxygen diffusion in the layered rock-salt structure. The oxygen-deficient phase shows extremely large 1st charge and discharge capacities of 388 and 305 mAh g^{-1}, respectively.

1. Introduction

Lithium-rich layered materials, $Li[Li_{1/3-x/3}Mn_{2/3-2x/3}M_x]O_2$ (M represents one or more transition metal elements), with $x < 1$, are promising candidates for positive electrodes of the next generation batteries, because of their high energy density, low cost and environmental benignity [1–7]. The structures of the lithium-rich layered materials are basically derived from the layered rock-salt α-$NaFeO_2$ type structure with space group $R\bar{3}m$. Additional Li ions occupy the transition metal (TM) layers, which results in an additional superstructure with the honeycomb Li/Mn ordering in the end member compound Li_2MnO_3 (alternatively described as $Li[Li_{1/3}Mn_{2/3}]O_2$ in the layered notation). All the lithium-rich compounds have a characteristic feature of a flat plateau-like region starting from 4.4 V vs. Li/Li^+ in the initial charge cycle. This process is however irreversible and is not observed in the initial discharge or subsequent cycles. The large discharge capacity is attributed to the activation of the Li_2MnO_3 components in the lithium-rich layered materials across the voltage plateau above 4.4 V at the initial charging process [6].

Significant efforts have been devoted to resolve the origin of this overcapacity for the lithium-rich phase. Since manganese ions predominantly exist in a tetravalent state without participating in charge compensation [8], other transition metal ions are considered to play a role in charge and discharge compensations [9–12]. On the other hand, manganese ions have been proposed to participate in discharge compensation according to the small changes observed in the Mn K-edge peak energy during the discharging process [11,12]. However, the large discharge capacity of the lithium-rich phase cannot be understood by the valence change estimated from the results of X-ray absorption spectroscopy. An

* Corresponding author. Tel./fax: +81 45 924 5401.
E-mail address: kanno@echem.titech.ac.jp (R. Kanno).

0378-7753/$ – see front matter © 2012 Elsevier B.V. All rights reserved.
doi:10.1016/j.jpowsour.2012.05.061

oxygen loss mechanism has also been proposed [3,13,14], which is supported by the oxygen gas generation and a decrease in the oxygen content in the grain observed by *in-situ* electrochemical mass spectroscopy measurements [15] and scanning transmission electron microscopy-electron energy-loss spectroscopy (STEM-EELS) [16], respectively. The total amount of oxygen gas produced from the electrode materials, however, is not consistent with the extra capacity obtained by the electrochemical cycling. Many other mechanisms that cause higher capacities have been proposed: rearrangements of transition metals and oxygen generation during lithium extraction cause the density of the material to increase [17,18]; and Li_2O extraction introduces lithium and oxygen vacancies in the structure [19]. Despite the experimental results of the lithium-rich layered materials, the mechanism that explains the large capacity after the 1st charging process is still ambiguous.

We focused on the host material, Li_2MnO_3, which is the end member of the solid solutions as well as the simplest system of the lithium-rich materials, and thus the most suitable material for understanding the mechanism of the electrochemical reactions. Although the Li_2MnO_3 phase has tetravalent manganese ions, the material shows charge–discharge characteristics with a 1st charge voltages of 4.4 V similar to the ternary lithium-rich layered compounds; several reaction mechanisms have also been proposed for Li_2MnO_3 including oxidation to Mn^{5+} [20], and simultaneous oxygen extraction during cycling and the exchange of Li^+ by H^+ linked to oxidation of electrolyte [21], which is also supported by the observation of oxygen gas generation observed by gas chromatography. The manganese has also been reported to be remained at the 4+ state during the 1st charging process and decreased during the 1st discharge process [22]. Okamoto recently examined the effect of oxygen vacancies in Li_2MnO_3 by first-principles calculations, which indicates that the oxygen vacancies favorably introduced at 8*j* site expand the lattice volume [23]. These previous results indicate extraction of a certain amount of oxygen in the 1st charging process, and that the oxygen-extracted phase might participate in the high discharge–charge capacity after the 2nd cycle. We therefore assumed that the high capacity of the lithium-rich layered materials is caused by oxygen extraction from the parent lattice, together with the reconstruction process to a phase suitable for the high capacity at the 1st charge process.

In the present study, we attempted to directly synthesize the oxygen-deficient phase from the starting material, Li_2MnO_3, using CaH_2 and LiH as strong reducing agents. The reducing agents, NaH and CaH_2, were reported to be efficient for the production of metastable materials having a structure with exotic coordination environment and/or valence state of transition metals; the oxygen deficient perovskite, $SrFeO_2$, with infinite-layer and a square coordination was obtained from $SrFeO_3$ with a cubic perovskite structure using CaH_2 as a reducing agent [24]. These reducing agents were also efficient in extracting oxygen from Li_2MnO_3 [25,26]. The oxygen deficient phase, Li_2MnO_{3-x}, was synthesized, and its structure, thermal behavior and electrochemical properties were investigated.

2. Experimental

Li_2MnO_3 was synthesized by a solid–state reaction with $LiOH{\cdot}H_2O$ (Kanto chemical, 98.0%) and $MnCO_3$ (High purity chemicals, 99.9%). The starting materials were mixed by mechanical milling in acetone for 1 h and dried in air. The powder was then pelletized and heated at 600 °C. The Li_2MnO_3 synthesized was mixed with CaH_2 (Sigma–Aldrich, 99.9%) or LiH (Alfa aesar, 99.4%) at a weight ratio of 1:2 or 1:4, placed into a glass tube, and heated at 255–265 °C for 6 h. To remove impurity phases (unreacted CaH_2 or LiH; CaO and Li_2O produced by the reaction) after the reaction, the samples were washed with methanol under an argon atmosphere and dried under vacuum at 120 °C overnight. These samples were characterized by powder X-ray diffraction measurements with Cu Kα radiation using a powder diffractometer (Rigaku SmartLab). Synchrotron X-ray diffraction patterns using a high-flux X-ray source were measured at the SPring-8 facility in a BL02B2 beam line. Synchrotron X-ray Rietveld analysis was used for structure determination with the Rietveld analysis program Rietan-FP [27]. The morphology of the products was characterized using a transmission electron microscope (TEM, JEOL JEM-2200FS) operated at 200 kV. The phase transition of the reduced phase was investigated by high temperature X-ray diffraction measurements. Thermogravimetric (TG) analysis was performed using a Rigaku Thermo plus instrument under an air gas flow. The electrochemical properties were measured using 2032 coin-type cells. The cathode material consisted of the active material, ketjen black, vapor grown carbon fiber (VGCF) and polyvinylidene fluoride (PVDF) at a gravimetric ratio of 80:8:2:10. The anode was metallic lithium. The electrolyte was 1 M $LiPF_6$ in a mixture of ethylene carbonate and diethyl carbonate (3:7 vol.%). Charge–discharge tests were carried out in the range of 2.0–4.6 V vs. Li/Li^+.

3. Results and discussion

Fig. 1 shows X-ray diffraction patterns of the samples reduced by CaH_2 and LiH, as well as the as-prepared samples, Li_2MnO_3. All the diffraction peaks of the pristine sample, Li_2MnO_3, are indexed by the layered rock-salt structure with space group *C*2/*m*. The broad superlattice peaks observed for Li_2MnO_3 between 20 and 30° (pattern (a) in Fig. 1) are caused by the ordering of Li and Mn ions in the $[Li_{1/3}Mn_{2/3}]$ layer. The broadening of these superlattice reflections is attributed to an increase in the amount of stacking faults perpendicular to the layered plane with decreasing reaction temperature. Li_2MnO_3 used for the reduction treatment has stacking faults. The diffraction pattern of the reduced sample of Li_2MnO_3 synthesized using CaH_2 (pattern (b) in Fig. 1) is also indexed by the layered rock-salt type structure. However, peak asymmetry observed especially for $20\bar{1}$ and 130 reflections, as well as $20\bar{2}$ and 131 reflections around 37 and 44°, respectively, indicate a multiphase character for the reduced phase. The diffraction patterns of

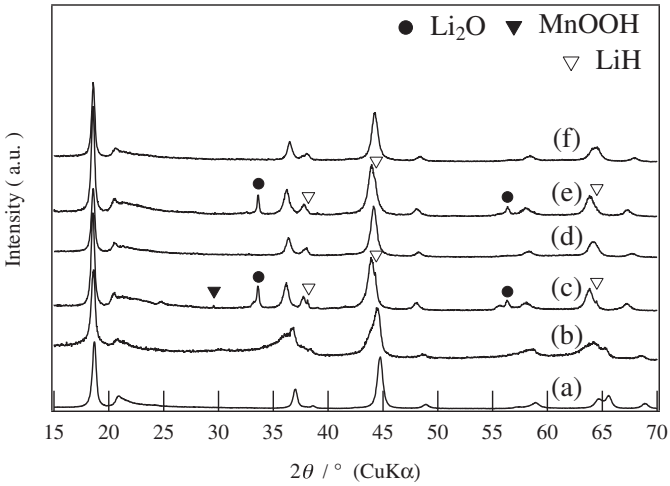

Fig. 1. X-ray diffraction patterns of Li_2MnO_3 and Li_2MnO_{3-x} synthesized at various reaction conditions. (a) Pristine Li_2MnO_3, (b) Li_2MnO_{3-x} synthesized from a mixture of Li_2MnO_3 and CaH_2 with a 1:2 M ratio, (c) Li_2MnO_{3-x} synthesized from a mixture of Li_2MnO_3 and LiH with a 1:4 M ratio before washing, (d) Li_2MnO_{3-x} after washing with methanol, (e) Li_2MnO_{3-x} synthesized using a mixture of Li_2MnO_3 and LiH with a 1:2 M ratio, and (f) Li_2MnO_{3-x} after washing with methanol.

the reaction products of the phases, Li_2MnO_{3-x} using a mixture of Li_2MnO_3 and LiH with a molar ratio of 1:4 or 1:2 (patterns (c) and (e) in Fig. 1) showed the same diffraction patterns similar to the layered rock-salt structure. The diffraction patterns of the samples after washing (pattern (d) and (f) in Fig. 1) show a mono-phasic character. These samples, Li_2MnO_3 and Li_2MnO_{3-x}, were subjected to X-ray diffraction analysis, TEM observation, TG analysis and electrochemical measurements.

The structures of Li_2MnO_3 before and after the reduction process were determined by the synchrotron X-ray diffraction data and the Rietveld analysis. The synchrotron X-ray diffraction data were refined based on a structure reported previously with cation mixing between Mn and Li ions [28]. A structure model with space group *C*2/*m* used for the refinement was as follows: Li1 and Mn1 in 2*b* (0, 0.5, 0); Li2 and Mn2 in 2*c* (0, 0, 0.5); Li3 and Mn3 in 4*h* (0, 0.6457(16), 0.5); Li4 and Mn4 in 4*g* (0, 0.1641(4), 0.0); O1 in 4*i* (0.2305(19), 0.0, 0.2273(15)); and O2 in 8*j* (0.2480(13), 0.3261(8), 0.2199(8)). Figs. 2 and 3 show the Rietveld analysis results for Li_2MnO_3 and its reduced sample, Li_2MnO_{3-x}, and Tables 1 and 2 summarize the *R* factors, lattice parameters and final structure parameters determined by the refinement process. All the diffraction peaks of Li_2MnO_3 and Li_2MnO_{3-x} are indexed by the space group *C*2/*m* except for the broad superlattice peaks observed between 8 and 13° (λ = 0.59866(3)). For Li_2MnO_3, the profile fittings provided a good agreement factor, R_{wp} of 5.19% (R_{Bragg} = 2.51%) with a goodness of fit value $S = R_{wp}/R_e$ = 1.18. For Li_2MnO_{3-x}, the fitting also provided an agreement factor, R_{wp} of 4.50% (R_{Bragg} = 2.40%) with $S = R_{wp}/R_e$ = 1.23. The cell parameters increased from a = 4.9304(5), b = 8.5391(6), c = 5.0259(4) Å, and β = 109.371(6)° to a = 4.981(2), b = 8.615(2), c = 5.0432(11) Å, and β = 109.46(3)° after the reduction process. The cation-mixing model was used to fit the layered structures. The occupation parameters of manganese ions in the 2*c* and 4*h* sites in the lithium layer are determined to be 0.0 for Li_2MnO_3, while the occupation parameter of manganese at the 2*c* site for Li_2MnO_{3-x} increased to 0.18(3), which indicates an increase in disordered arrangements after the reducing reaction. The occupancy parameters at the oxygen 4*i* and 8*j* sites changed from1.0 and 1.0 to 1.0 and 0.92(9), for Li_2MnO_3 and Li_2MnO_{3-x}, respectively. These results indicate an increase in the oxygen vacancy at the 8*j* site with the reduction reaction. The lattice volume expanded with the introduction of oxygen vacancies at the 8*j* site without changes in its original layered structure after the reduction process, which is in good agreements with the results obtained by first-principles calculations [23]. The results obtained by the synchrotron X-ray diffraction data were confirmed by our neutron diffraction measurements using the lithium isotope, $^7Li_2MnO_3$.

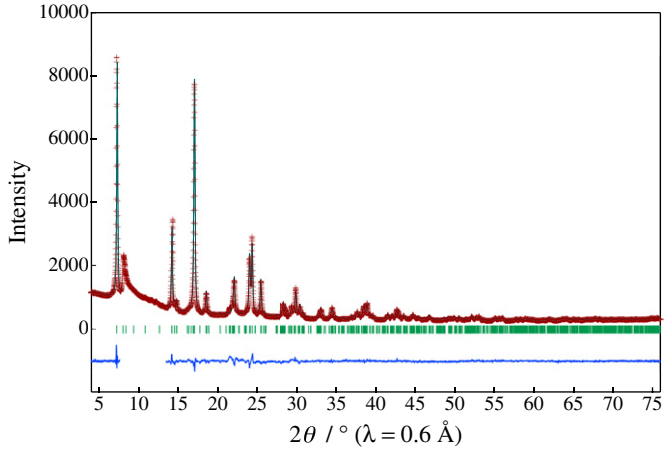

Fig. 2. Observed (+), calculated (solid dark green line) and difference plots (solid blue line) for the synchrotron X-ray Rietveld analysis of the Li_2MnO_3 synthesized at 600 °C. (For interpretation of the references to colour in this figure legend, the reader is referred to the web version of this article.)

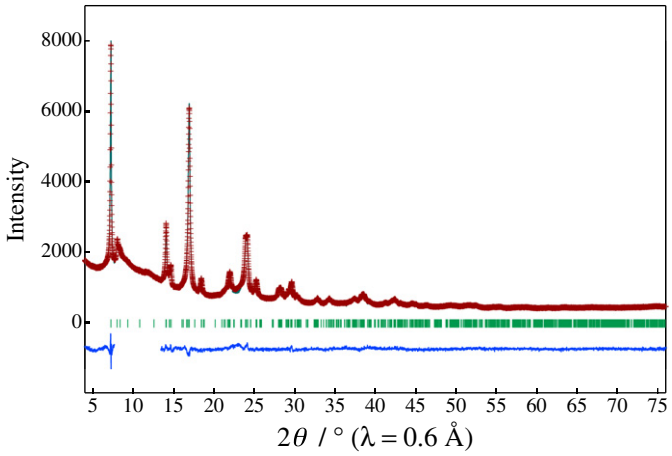

Fig. 3. Observed (+), calculated (solid dark green line) and difference plots (solid blue line) for the synchrotron X-ray Rietveld analysis of the reduced sample, Li_2MnO_{3-x} synthesized by the reaction with Li_2MnO_3 and LiH at a molar ratio of 1:4. (For interpretation of the references to colour in this figure legend, the reader is referred to the web version of this article.)

The morphologies of Li_3MnO_3 and the oxygen deficient phase, Li_2MnO_{3-x}, were examined by transmission electron microscopy (TEM). Fig. 4 (a) and (b) shows the high-resolution TEM images of Li_2MnO_3 and Li_2MnO_{3-x}, respectively. The particle size observed in the TEM images was around 50 nm for both Li_2MnO_3 and Li_2MnO_{3-x}; no significant changes in the particle size were found after the reduction process with LiH. This is consistent with the X-ray diffraction results in which no significant peak broadening was observed after the reduction reaction. The lattice images of both Li_2MnO_3 and Li_2MnO_{3-x} shown in Fig. 4 (c) and (d), respectively are characteristics of the layered structure, which indicates no changes in the layered structure after the reduction process. The *c* axis parameter calculated using the hexagonal system increased from 14.04 to 14.67 Å with the reduction process, which is consistent with the results of the structure analysis. Although Li_2MnO_3 showed a periodic lattice image, which is an indicative of a layered structure, large disorder in the layered stacking was observed for Li_2MnO_{3-x}. The reduction process introduced the oxygen vacancy and thus caused the high disordered arrangements and/or stacking faults in the layered structure.

Thermal behavior of the oxygen deficient phase was examined by high temperature X-ray diffraction measurements and TG analysis. Fig. 5 shows the high-temperature synchrotron X-ray diffraction patterns of Li_2MnO_{3-x} measured from room temperature to 550 °C and then down to room temperature. Fig. 6 shows the

Table 1
Synchrotron Rietveld refinement results for Li_2MnO_3.

Atom	Site	*g*	*x*	*y*	*z*	*B*/Å^2
Li(1)	2*b*	0.657(7)	0.0	0.5	0.0	0.5
Mn(1)	2*b*	= 1 − *g*(Li(1))	0.0	0.5	0.0	0.5
Li(2)	2*c*	1.0	0.0	0.0	0.5	1.0
Li(3)	4*h*	1.0	0.0	0.6457(17)	0.5	1.0
Li(4)	4*g*	0.149(5)	0.0	0.1641(4)	0.0	0.5
Mn(2)	4*g*	= 1 − *g*(Li(4))	0.0	= *y*(Li(4))	0.0	0.5
O(1)	4*i*	1.0	0.2305(19)	0.0	0.2273(15)	0.8
O(2)	8*j*	1.0	0.2480(13)	0.3261(8)	0.2199(8)	0.8

Unit cell: monoclinic *C*2/*m* (12); a = 4.9304(5) Å, b = 8.5391(6) Å, c = 5.0259(4) Å, β = 109.371(6)°, R_{wp} = 5.19, R_p = 3.98, $S = R_{wp}/R_e$ = 1.18, R_B = 2.51, R_F = 1.70.

Table 2
Synchrotron Rietveld refinement results for the reduced sample, Li_2MnO_{3-x}.

Atom	Site	g	x	y	z	B/Å^2
Li(1)	2*b*	0.25(6)	0.0	0.5	0.0	0.5
Mn(1)	2*b*	= 1 − *g*(Li(1))	0.0	0.5	0.0	0.5
Li(2)	2*c*	0.82(3)	0.0	0.0	0.5	1.0
Mn(2)	2*c*	= 1 − g(Li(2))	0.0	0.0	0.5	1.0
Li(3)	4*h*	1.0	0.0	0.684(4)	0.5	1.0
Li(4)	4*g*	0.34(5)	0.0	0.1786(5)	0.0	0.5
Mn(3)	4*g*	= 1 − *g*(Li(4))	0.0	= *y*(Li(4))	0.0	0.5
O(1)	4*i*	1.0	0.209(4)	0.0	0.241(4)	0.8
O(2)	8*j*	0.92(9)	0.262(4)	0.3363(19)	0.2199(19)	0.8

Unit cell: monoclinic *C*2/*m* (12); $a = 4.981(2)$ Å, $b = 8.615(2)$ Å, $c = 5.0432(11)$ Å, $\beta = 109.46(3)^\circ$, $R_{wp} = 4.50$, $R_p = 3.52$, $S = R_{wp}/R_e = 1.23$, $R_B = 2.40$, $R_F = 1.24$.

TG curves from room temperature to 600 °C and then down to room temperature. The dots on the TG curve in Fig. 6 correspond to the temperatures measured by the high temperature X-ray diffraction analysis shown in Fig. 5. The diffraction peaks around 14° in Fig. 5 are indexed as $20\bar{1}$ and 130 reflections with space group *C*/2*m*. From room temperature to 230 °C, an increase in weight was observed together with a peak shift to higher angles, corresponding to a decrease in the lattice parameters. Oxygen then reinserted again into the bulk structure of Li_2MnO_{3-x} with increasing temperature. This clearly indicates that the phase obtained by the reduction process with LiH has an oxygen deficient composition, and the oxygen deficient phase has larger lattice parameters. The amount of oxygen calculated by the weight gain was 0.19 mol, corresponding to the oxygen non-stoichiometry *x* in Li_2MnO_{3-x}. From 230 to 450 °C, a weight loss was observed together with an increase in the lattice parameters. Above 450 °C, the peak around 14° splits into two which might have been caused by a phase separation from the layered phase to a cubic phase and a monoclinic phase. In order to confirm the phase separation, the structure of the cubic phase was refined by synchrotron Rietveld analysis. The cubic phase is indexed as a spinel type structure with space group $Fd\bar{3}m$. Fig. 7 shows the Rietveld refinement pattern of the phase measured at room temperature after heating to 550 °C. The profile fittings provided a good agreement factor, R_{wp} of 4.43% with $S = R_{wp}/R_e = 0.88$. These results indicate that the oxygen deficient phase decomposed at higher temperatures with the cubic spinel and the layered rock-salt phases. The thermal behaviors obtained in the present study are summarized as follows: the oxygen deficient phase of Li_2MnO_{3-x} was obtained by the reduction with LiH. The composition *x* was determined to be 0.19 by the TG measurements. During the heating process from room temperature to 600 °C, the oxygen deficient phase absorbed oxygen into the bulk structure from room temperature to 230 °C. Above 230 °C, the phase decomposed into two phases, the layered- and spinel-type phases, with a loss of oxygen again from the structure.

The charge–discharge characteristics of the oxygen deficient phase were investigated. Fig. 8 shows the charge–discharge curves for Li_2MnO_3 and Li_2MnO_{3-x}. An initial charge plateau was observed above 4.4 V for Li_2MnO_3. On the other hand, no significant plateau was observed at the 1st charge of the oxygen deficient Li_2MnO_{3-x} phase. The oxygen deficient phase showed better electrochemical performances than Li_2MnO_3. Fig. 9 shows the rate performance of the oxygen deficient phase. The Li_2MnO_{3-x} showed a discharge capacity of 310 mAh g^{-1} at a current density of 10 mA g^{-1}, and the discharge capacity decreased to 60 mAh g^{-1} with increasing current density to 3 A g^{-1}. Although the reduced phase showed good cycling characteristics, a gradual decrease in the capacity was observed with cycling. Previously, the stepwise charging was reported to improve the lithium excess phase with the ternary system $Li[Li_{1/3-x/3}Mn_{2/3-2x/3}M_x]O_2$ [5]. Similar charging process was examined for the oxygen deficient phase, Li_2MnO_{3-x}; the charge–discharge curves after the stepwise charging are shown in Fig. 10. The charge capacity gradually increased, and after charging to 200 mAh g^{-1}, which corresponds to a charge voltage of 4.3 V, the

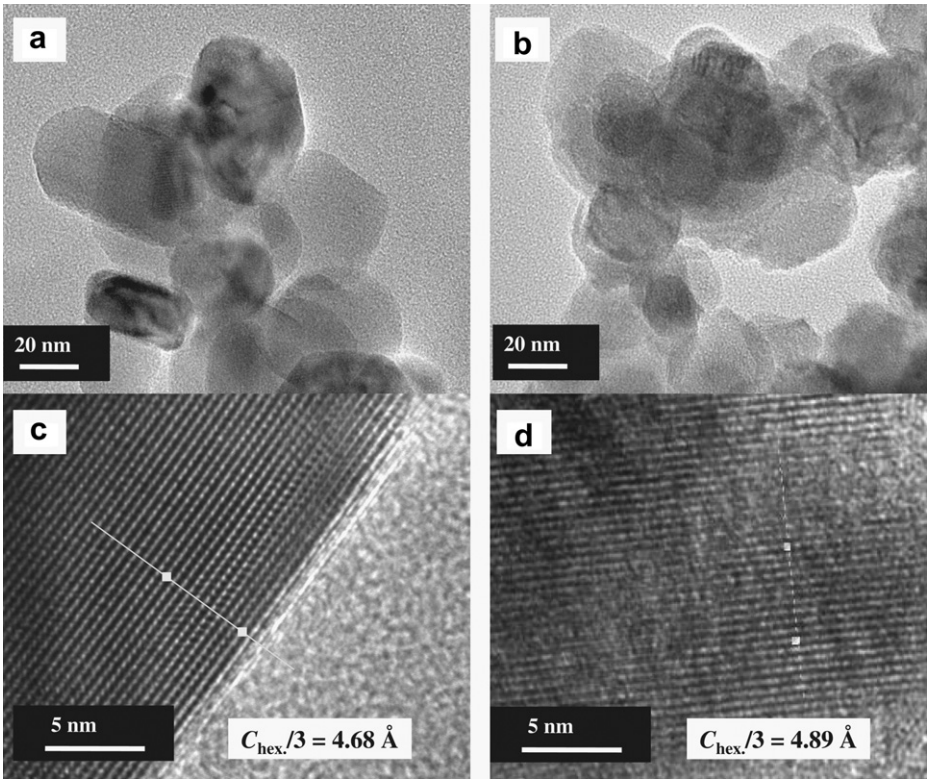

Fig. 4. High-resolution TEM images for (a) as-prepared Li_2MnO_3, (b) reduced Li_2MnO_{3-x} sample, as well as magnified images for (c) Li_2MnO_3 and (d) reduced Li_2MnO_{3-x}.

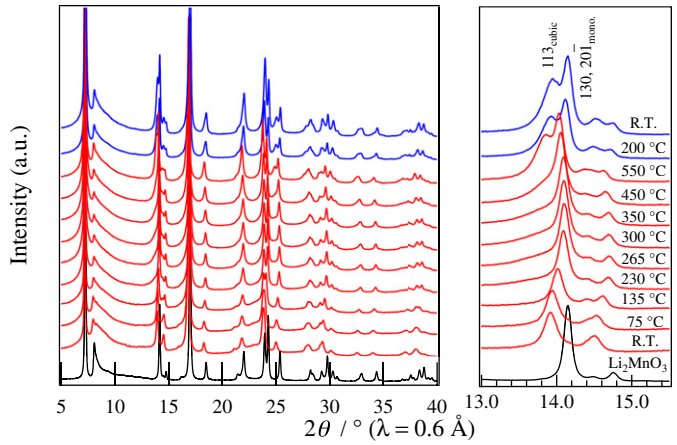

Fig. 5. High-temperature synchrotron X-ray diffraction patterns for the reduced sample, Li_2MnO_{3-x}.

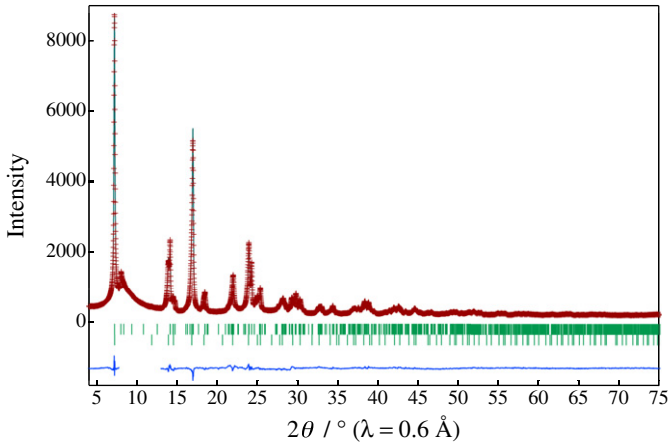

Fig. 7. Observed (+), calculated (solid dark green line) and difference plots (solid blue line) for the synchrotron Rietveld analysis of the reduced sample, Li_2MnO_{3-x}, measured at room temperature after heating to 550 °C. (For interpretation of the references to colour in this figure legend, the reader is referred to the web version of this article.)

sample showed a discharge capacity of 190 mAh g^{-1}. The plateau region at 4.4 V disappeared for the stepwise charged samples. This indicates that the structure rearrangement proceeded during the lithium intercalation and the material after the structure rearrangement showed good reversibly.

The direct synthesis of the oxygen deficient phase has been attempted over the past years. Changing the reaction conditions has lead to only 1% oxygen loss from the stoichiometric Li_2MnO_3 [29]. The annealing process for $Li_{1.12}Mn_{0.55}Ni_{0.145}Co_{0.1}O_2$ in H_2 was also provided the 1st charge plateau, which is attributed to the oxygen extraction process above 4.4 V [30]. The present study revealed the extraction of oxygen from the lithium-rich layered composition, Li_2MnO_3 by the LiH treatment, and the charge–discharge curves of the reduced phase with a composition, Li_2MnO_{3-x} ($0 < x < 0.19$), showed no plateau region above 4.4 V. The layered rock-salt oxides cathodes with a lithium-rich composition were reported to be activated by the 1st charging process and this process was characterized by a plateau region above 4.4 V. The reaction during the 1st charge might be an oxygen extraction and thus caused structure reconstruction to produce a structure suitable for extremely high charge–discharge capacities. The present results indicate that the voltage plateau in the 1st charge corresponds to an oxygen extraction reaction, and the high capacitive phase obtained for the $Li[Li_{1/3-x/3}Mn_{2/3-2x/3}M_x]O_2$

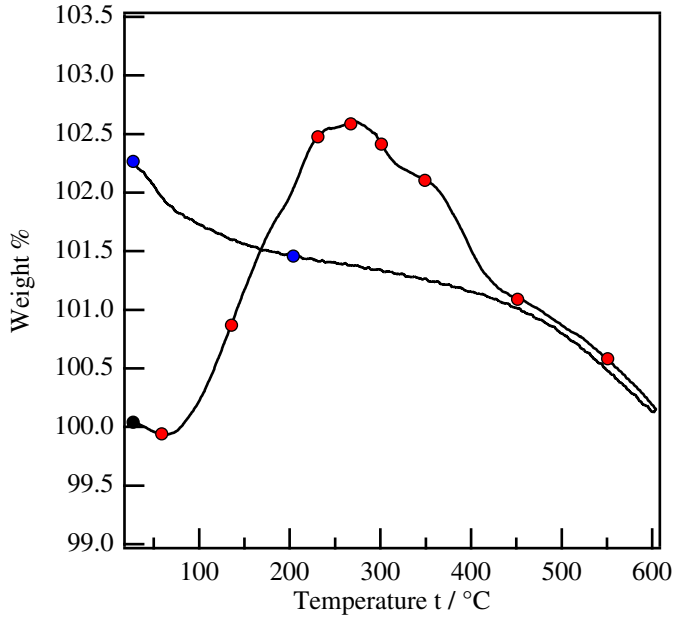

Fig. 6. TG curve for the reduced sample, Li_2MnO_{3-x}. The dots indicated in the figure correspond to the temperature measured by X-ray diffraction shown in Fig. 5.

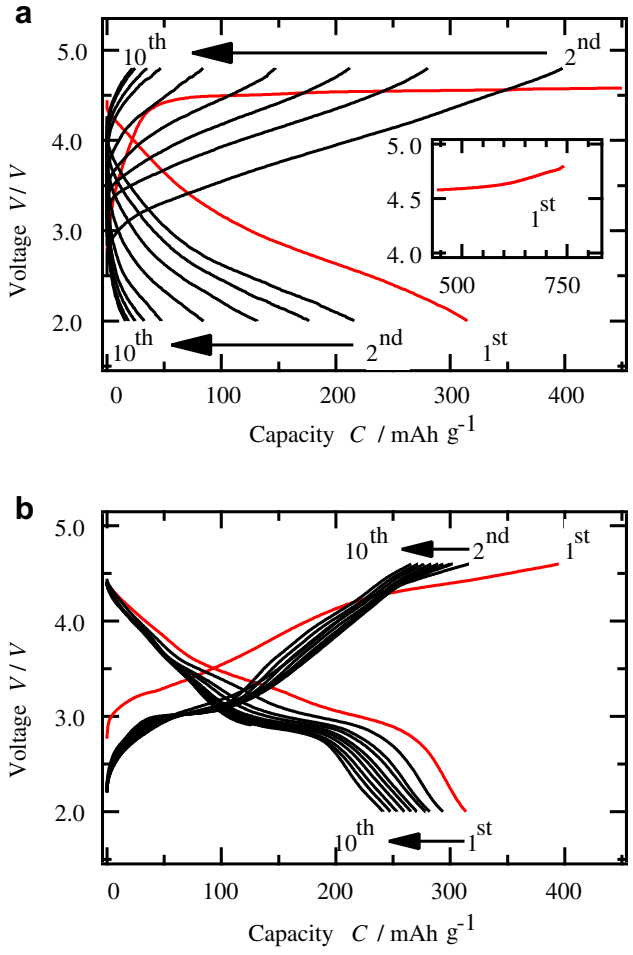

Fig. 8. (a) Charge–discharge curves for Li_2MnO_3 with a voltage range 2.0–4.8 V and (b) for the reduced sample, Li_2MnO_{3-x}, at a rate of 10 mA g^{-1} with a voltage range 2.0–4.6 V.

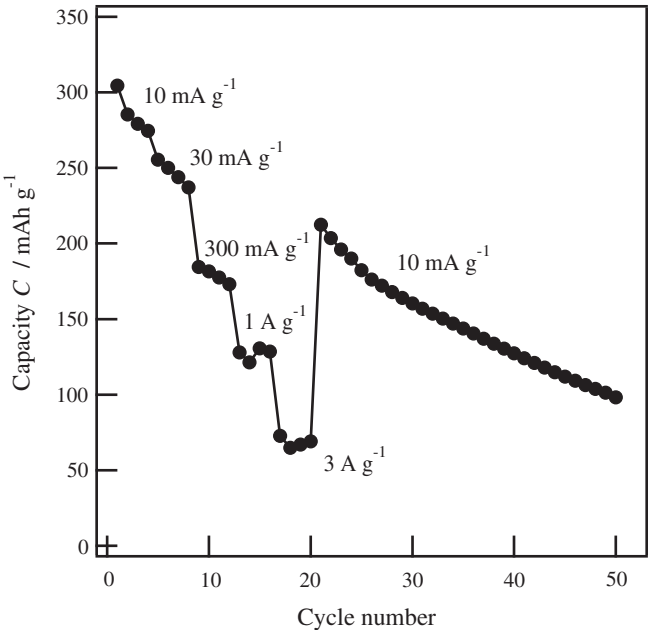

Fig. 9. Rate performance of the reduced sample with a voltage range of 2.0–4.6 V.

phase might have oxygen vacancy. However, the stepwise charging for the oxygen deficient phase, Li_2MnO_{3-x}, improved the charge–discharge characteristics, which indicates that the oxygen deficient phase obtained by the thermal treatment is not sufficient to obtain the highest charge–discharge characteristics for the lithium-rich layered materials. The oxygen deficient phase was found to contain a structure disorder either in the layered configuration (stacking fault, for example), or disordered arrangements in the oxygen packing by the TEM measurements. These disordered structures might transform to a structure suitable for charge–discharge characteristics at the 1st charging process without showing voltage plateaus, and the new structure obtained by the 1st charge might be easier to be obtained by the stepwise charging. Further studies on the structure rearrangements from the oxygen deficient phase to a phase showing high charge–discharge capacity are necessary.

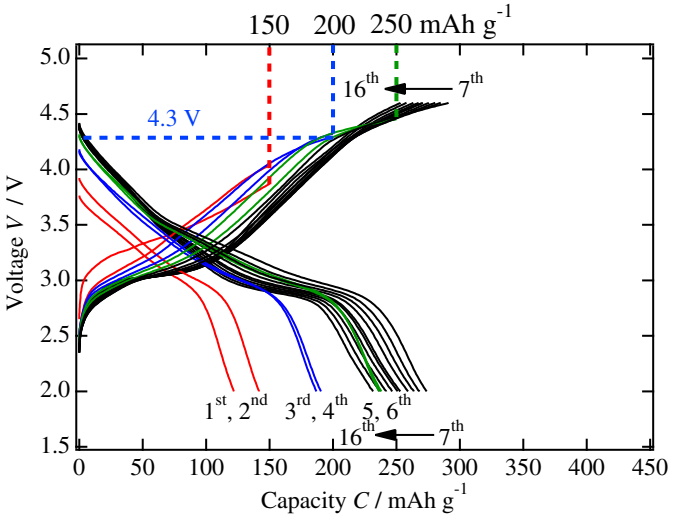

Fig. 10. Charge–discharge curves for the reduced sample with stepwise charging. The restricted charge capacities were increased every 2 cycles from 150 to 250 mAh g^{-1}.

4. Conclusions

The new oxygen deficient phase, Li_2MnO_{3-x}, was synthesized by heating a mixture of Li_2MnO_3 and CaH_2/LiH. The new reduced phase was an oxygen-deficient phase, which was confirmed by the TG and the structure analyses. The TEM images of the reduced phase showed a disordered arrangement of the layered structure, while the X-ray diffraction patterns were characteristics for the layered rock-salt structure. The charge–discharge characteristics of Li_2MnO_{3-x} were quite different from the parent material, Li_2MnO_3. The structure changes and reaction mechanism of the lithium-rich layered materials are summarized as follows.

(i) Low temperature reduction with metal hydride caused the extraction of oxygen from the bulk structure, leading to the oxygen deficient phase.
(ii) The reduction process introduced a disordered arrangement in the layered structure, which was observed by the TEM measurements and structure analysis.
(iii) Reversible oxygen re-insertion was observed by heating in air.
(iv) The initial charge process of the oxygen deficient phase showed no plateau at the 4.4 V region, indicating that the plateau at the voltage region for Li_2MnO_3 corresponds to the oxygen extraction process.

Acknowledgements

This work was supported by a Grant-in-Aid for Scientific Research (A). The synchrotron X-ray diffraction experiments were performed at the BL02B2 beam line at the SPring-8 facility with the approval of the Japan Synchrotron Radiation Research Institute (JASRI) (proposal nos. 2010B1693, 2011A1612).

References

[1] K. Numata, C. Sakaki, S. Yamanaka, Solid State Ionics 117 (1999) 257–263.
[2] T. Ohzuku, Y. Makimura, Chem. Lett. 30 (2001) 744–745.
[3] Z.H. Lu, D.D. MacNeil, J.R. Dahn, Electrochem. Solid State Lett. 4 (2001) A191–A194.
[4] M.M. Thackeray, S.H. Kang, C.S. Johnson, J.T. Vaughey, R. Benedek, S.A. Hackney, J. Mater. Chem. 17 (2007) 3112–3125.
[5] A. Ito, D. Li, Y. Ohsawa, Y. Sato, J. Power Sources 183 (2008) 344–346.
[6] T. Ohzuku, M. Nagayama, K. Tsuji, K. Ariyoshi, J. Mater. Chem. 21 (2011) 10179–10188.
[7] S.K. Martha, J. Nanda, G.M. Veith, N.J. Dudney, J. Power Sources 199 (2012) 220–226.
[8] M. Balasubramanian, J. McBreen, I.J. Davidson, P.S. Whitfield, I. Kargina, J. Electrochem. Soc. 149 (2002) A176–A184.
[9] J.R. Croy, M. Balasubramanian, D. Kim, S.-H. Kang, M.M. Thackeray, Chem. Mater. 23 (2011) 5415–5424.
[10] G.-Y. Kim, S.-B. Yi, Y.J. Park, H.-G. Kim, Mater. Res. Bull. 43 (2008) 3543–3552.
[11] A. Ito, Y. Sato, T. Sanada, M. Hatano, H. Horie, Y. Ohsawa, J. Power Sources 196 (2011) 6828–6834.
[12] N. Yabuuchi, K. Yoshii, S.-T. Myung, I. Nakai, S. Komaba, J. Am. Chem. Soc. 133 (2011) 4404–4419.
[13] Z.H. Lu, L.Y. Beaulieu, R.A. Donaberger, C.L. Thomas, J.R. Dahn, J. Electrochem. Soc. 149 (2002) A778–A791.
[14] A.D. Robertson, P.G. Bruce, Electrochem. Solid State Lett. 7 (2004) A294–A298.
[15] A.R. Armstrong, M. Holzapfel, P. Novak, C.S. Johnson, S.H. Kang, M.M. Thackeray, P.G. Bruce, J. Am. Chem. Soc. 128 (2006) 8694–8698.
[16] J. Kikkawa, T. Akita, M. Tabuchi, K. Tatsumi, M. Kohyama, J. Electrochem. Soc. 158 (2011) A760–A768.
[17] N. Tran, L. Croguennec, M. Menetrier, F. Weill, P. Biensan, C. Jordy, C. Delmas, Chem. Mater. 20 (2008) 4815–4825.
[18] M. Jiang, B. Key, Y.S. Meng, C.P. Grey, Chem. Mater. 21 (2009) 2733–2745.
[19] Y.-S. Hong, Y.J. Park, K.S. Ryu, S.H. Chang, Solid State Ionics 176 (2005) 1035–1042.
[20] P. Kalyani, S. Chitra, T. Mohan, S. Gopukumar, J. Power Sources 80 (1999) 103–106.
[21] A.D. Robertson, P.G. Bruce, Chem. Mater. 15 (2003) 1984–1992.
[22] D.Y.W. Yu, K. Yanagida, Y. Kato, H. Nakamura, J. Electrochem. Soc. 156 (2009) A417–A424.
[23] Y. Okamoto, J. Electrochem. Soc. 159 (2012) A152–A157.

[24] Y. Tsujimoto, C. Tassel, N. Hayashi, T. Watanabe, H. Kageyama, K. Yoshimura, M. Takano, M. Ceretti, C. Ritter, W. Paulus, Nature 450 (2007) 1062–U1068.
[25] T. Kaneko, H. Ochiai, M. Nagao, A. Yamada, R. Kanno, Abstracts of the 76th Annual Meeting of Electrochemical Society of Japan, Kyoto, Japan (2009) 1O10.
[26] K. Kubota, S. Ando, T. Kaneko, H.M. Chang, M. Hirayama, R. Kanno, Y. Imanari, K. Nakane, Abstracts of the 5th Asian Conference on Electrochemical Power Sources (ACEPS), Singapore (2010) pp. 98–99.
[27] F. Izumi, K. Momma, Solid State Phenom. 130 (2007) 15–20.
[28] A. Boulineau, L. Croguennec, C. Delmas, F. Weill, Chem. Mater. 21 (2009) 4216–4222.
[29] D. Pasero, V. McLaren, S. de Souza, A.R. West, Chem. Mater. 17 (2005) 345–348.
[30] A. Abouimrane, O.C. Compton, H. Deng, I. Belharouak, D.A. Dikin, S.T. Nguyen, K. Amine, Electrochem. Solid State Lett. 14 (2011) A126–A129.